Photochemistry of polycyclic aromatic hydrocarbons in cosmic water ice

II. Near UV/VIS spectroscopy and ionization rates

J. Bouwman[1,4], H. M. Cuppen[1], M. Steglich[2], L. J. Allamandola[3], and H. Linnartz[1]

[1] Raymond and Beverly Sackler Laboratory for Astrophysics, Leiden Observatory, Leiden University, PO Box 9513, 2300 RA Leiden, The Netherlands
e-mail: bouwman@berkeley.edu
[2] Laboratory Astrophysics Group of the Max Planck Institute for Astronomy at the Friedrich Schiller University Jena, Institute of Solid State Physics, Helmholtzweg 3, 07743 Jena, Germany
[3] NASA-Ames Research Center, Space Science Division, Mail Stop 245-6, Moffett Field, CA 94035, USA
[4] Current address: Departments of Chemistry and Physics, University of California, Berkeley, California 94720, USA

ABSTRACT

Context. Mid-infrared emission features originating from polycyclic aromatic hydrocarbons (PAHs) are observed towards photon dominated regions in space. Towards dense clouds, however, these emission features are quenched. Observations of dense clouds show that many simple volatile molecules are frozen out on interstellar grains, forming thin layers of ice. Recently, observations have shown that more complex non-volatile species, presumably including PAHs, also freeze out and contribute to the ongoing solid-state chemistry.
Aims. The study presented here aims at obtaining reaction rate data that characterize PAH photochemistry upon vacuum ultraviolet (VUV) irradiation in an interstellar H_2O ice analogue to explore the potential impact of PAH:H_2O ice reactions on overall interstellar ice chemistry. To this end, the experimental results are implemented in a chemical model under simple interstellar cloud conditions.
Methods. Time-dependent near-UV/VIS spectroscopy on the VUV photochemistry of anthracene, pyrene, benzo[ghi]perylene and coronene containing interstellar H_2O ice analogs is performed at 25 and 125 K, using an optical absorption setup.
Results. Near-UV/VIS absorption spectra are presented for these four PAHs and their photoproducts including cationic species trapped in H_2O ice. Oscillator strengths of the cation absorption bands are derived relative to the oscillator strength of the neutral parent PAH. The loss of the parent and growth of PAH photoproducts are measured as a function of VUV dose, yielding solid state reaction constants. The rate constants are used in an exploratory astrochemical model, to assess the importance of PAH:H_2O ice photoprocessing in UV exposed interstellar environments, compared with the timescales in which PAH molecules are incorporated in interstellar ices.
Conclusions. All four PAHs studied here are found to be readily ionized upon VUV photolysis when trapped in H_2O ice and exhibit similar rates for ionization at astronomically relevant temperatures. Depending on the relative efficiency of H_2O photodesorption and PAH photoionization in H_2O ice, the latter may trigger a charge induced aromatic solid state chemistry, in which PAH cations play a central role.

Key words. astrochemistry – molecular processes – methods: laboratory – techniques: spectroscopic – ISM: molecules

1. Introduction

The presence of polycyclic aromatic hydrocarbons (PAHs) in many phases of the interstellar medium is evidenced by their strong and ubiquitous mid-infrared (mid-IR) emission features (Smith et al. 2007; Draine et al. 2007; Draine & Li 2007; Tielens 2008). Mid-IR features are efficiently emitted by a PAH after excitation by an energetic photon. Toward dense clouds, however, these mid-IR features are strongly quenched. Here, most volatile molecules are frozen out on grains forming layers of ice (e.g., Pontoppidan et al. 2004; Boogert et al. 2008; Öberg et al. 2008; Bottinelli et al. 2010). Under such conditions, less volatile molecules such as PAHs condense on interstellar grains as well, incorporating them in interstellar ices.

Indeed, weak mid-IR absorption features in the spectra of dense clouds point to the presence of PAHs in these ices as well, with PAH:H_2O ice concentrations on the order of a few percent (Smith et al. 1989; Sellgren et al. 1995; Brooke et al. 1999; Chiar et al. 2000; Bregman et al. 2000). Based on these observations, Bouwman et al. (2011) deduced PAH:H_2O ice ratios toward MonR2/IRS3 to be about 2%, a ratio comparable to common interstellar ice species such as H_2CO and OCN^-. However, since astronomical PAHs are expected to contain on the order of 50 to 100 C atoms and some 20 to 30 reactive C–H peripheral sites, their influence on interstellar ice chemistry and ice physics is likely important.

Experimental studies on the effect of vacuum ultraviolet (VUV) irradiation of interstellar ice analogues have shown that more complex molecules form in the simplest mixed ices (e.g. Gerakines et al. 1995; Öberg et al. 2009a; Muñoz Caro & Dartois 2009). Laboratory studies on VUV irradiated PAH containing ices indicated that PAHs are easily ionized (Gudipati & Allamandola 2003; Gudipati 2004; Bouwman et al. 2009, 2010). These experiments also showed the formation of new species. Kinetic information on these chemical reactions, however, is largely lacking.

Here, we present the time evolution of the use-up of four PAHs, anthracene (Ant, $C_{14}H_{10}$), pyrene (Py, $C_{16}H_{10}$), benzo[ghi]perylene ($B_{ghi}P$, $C_{22}H_{12}$), and coronene (Cor, $C_{24}H_{12}$) in H_2O ice together with the formation and destruction of the ionized PAH^+ species. This paper is part II of a series which aims to quantify and understand the time-dependent chemistry of $PAH:H_2O$ ice mixtures upon VUV irradiation and the resulting photoproducts. Part I deals with the mid-IR spectroscopy of the photoproducts and its applications to astronomical observations of low and high mass objects and has been published separately (Bouwman et al. 2011). Because of severe band overlap, the infrared experiments are not capable of providing the kinetic information reported here. The two papers together provide a complementary (vibrational and electronic) study of PAH containing H_2O ice, as well as their photoproducts and dynamic behavior upon VUV excitation.

Here, the chemical evolution is tracked by means of near-UV/VIS absorption spectroscopy at two temperatures, 25 K and 125 K. This work is an extension of a previous optical study of pyrene in H_2O ice (Bouwman et al. 2010) and draws more general conclusions on PAH photochemistry in ices based on a larger set of different PAHs. Furthermore, the present work extends the $PAH:H_2O$ photochemistry to larger and astrophysically more relevant members of the PAH family.

The outline of this paper is as follows. In Sect. 2 the experimental setup is briefly discussed, together with details of supporting calculations. Section 3 describes spectra of the PAH and PAH^+ cations, the assignments of the observed transitions and presents the (relative) oscillator strengths. The fitted time-dependent data are discussed in detail in Sect. 4, after which the astrophysical implications are discussed in Sect. 5. The conclusions are summarized in Sect. 6.

2. Experimental technique

The experimental details are available from Bouwman et al. (2009). The heart of the setup is of a high-vacuum ($\sim 10^{-7}$ mbar) chamber. In the center of the vacuum chamber a MgF_2 sample window is suspended, which is cooled by a closed cycle He cryostat to a temperature of 25 K. Temperatures as low as 11 K can be realized. PAH containing H_2O ices are grown onto the sample window by vapor deposition. Milli-Q H_2O is further purified by three freeze-pump-thaw cycles and the PAHs are used as commercially available (Ant, Aldrich $\geq$99%, Py, Aldrich, 99%, $B_{ghi}P$, Aldrich, 98%, Cor, Aldrich, 99%). The thickness of the ice samples is determined by laser interference and the amount of deposited PAH is monitored in absorption.

The inlet system has been modified for depositing the larger PAHs in our sample, $B_{ghi}P$ and Cor. A sample container is mounted in the vacuum chamber and located adjacent to the H_2O deposition tube. The sample container is heated with polyimide insulated nichrome heater wire. The H_2O exposure is set to result in a growth rate of approximately $4\ \mu m\ h^{-1}$. The current through the heater wire determines the PAH sample temperature and thus the resulting sample concentration. It should be noted that, in view of the higher sensitivity of the optical detection scheme compared to the infrared, these concentrations are much lower than in Paper I.

After deposition on the 25 K window, the sample is heated to the desired temperature. Subsequently, the sample is subject to VUV radiation, which is produced by a H_2 flow microwave (MW) discharge lamp. The lamp operates at a static H_2 pressure of 0.4 mbar and a MW power of 100 W, resulting in an effective VUV flux of $\sim 10^{14}$ photons $cm^{-2}\ s^{-1}$ at the sample surface

(Muñoz Caro et al. 2002). In the present experiment this value may be higher as a reflecting tube has been positioned behind the lamp also directing diverging photons towards the ice sample. As an upper limit we use a flux of 10^{15} photons $cm^{-2}\ s^{-1}$ in this paper.

Near UV/VIS absorption spectra are taken during VUV processing of the samples. To this end, a Xe-lamp is used as a broadband light source and a spectrometer equipped with a 1024×256 pixel CCD camera is used as detector. The CCD camera is read out in vertical binning mode by a computer on which the raw data are converted into optical depth ($OD = \ln(I/I_0)$). Spectra ranging from $\sim$280 to 800 nm are taken at a rate of $0.1\ s^{-1}$, which is sufficient to monitor chemical changes in our ice samples. Each spectrum is the result of co-adding 229 individual spectra, resulting in a high signal-to-noise ratio.

The integrated absorbance of the deposited neutral PAH signal, $\int \tau_\nu d\nu$, is converted into a PAH column density, N_{PAH}, via the oscillator strength of the neutral PAH, f, and the conversion factor 8.88×10^{-13} taken from Kjaergaard et al. (2000):

$$N_{PAH} = \frac{\int \tau_\nu d\nu}{8.88 \times 10^{-13} f}. \tag{1}$$

Together with an ice thickness measurement based on the interference pattern in the reflection of a HeNe laser as described in Bouwman et al. (2009), this allows for a determination of the $PAH:H_2O$ concentration. Sample deposition is stopped at thicknesses of $\sim$2 μm, resulting in comparable ice samples.

In a typical 4 h experiment, as many as 1400 spectra are obtained. The spectra are all baseline corrected by fitting a second-order polynomial through points where no absorptions occur and subtracting the polynomial. Additionally, absorption bands are integrated and, if necessary, corrected for contributions by atomic H lines of the H_2 MW discharge lamp. All the data handling is performed in a LabView program.

In order to support the assignment of the measured absorption photoproduct bands, density functional theory (DFT) calculations are performed using the GAUSSIAN09 software (Frisch et al. 2009). The B3LYP functional is used in conjunction with the 6-311++G(2d, p) basis set to determine the ground state geometry and electronic structure of PAH neutrals and cations as a starting point to predict the electronic transitions. Excited states are investigated within the framework of the time-dependent density functional theory (TDDFT) applying the same level of theory.

3. $PAH:H_2O$ spectroscopy

Long duration photolysis experiments are performed on a set of four PAHs (Ant, Py, $B_{ghi}P$, and Cor) in H_2O ice at low (25 K) and high (125 K) sample temperatures. An overview of the used mixture concentrations, the temperature at which the samples are photolyzed, and the oscillator strength values (f) of the neutral PAHs adopted from the literature is given in Table 1.

For each of the PAHs under investigation, the oscillator strength of the cation absorption bands relative to that of the neutral precursor is determined. This allows for a full quantitative study of the formation and destruction, which will be presented in Sect. 4. Relative oscillator strengths are determined by plotting the time evolution of the integrated absorbance of the cation transition against the integrated absorbance of the strongest electronic transition of the neutral species (see Fig. 1). Both integrated absorbances are normalized to the amount of deposited neutral PAH, which is determined during the preparation of the ice sample. A quantitative conversion of the PAH molecule into
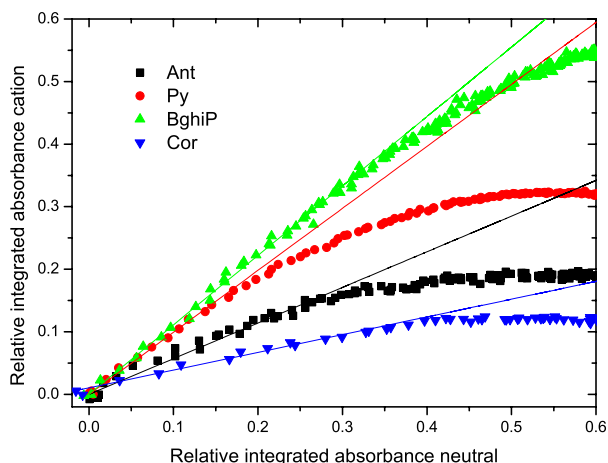
Fig. 1. The correlation between the amount of cation produced and the amount of neutral consumed, both relative to the total amount of deposited neutral precursor; Ant, Py, $B_{ghi}P$, or Cor.

Table 1. Overview of the used PAH species, PAH:H_2O concentrations, sample temperatures, the integration intervals[a], and corresponding oscillator strengths[b].

Species	Conc.	T_{Sample} (K)	λ_{range} (nm)	f
Ant	1:2,000	25	316–385	0.1[c]
Ant	1:1,500	25		
Ant	1:900	25		
Ant	1:500	125		
Py	1:5,000	25	290–345	0.33[d]
Py	1:6,500	125		
$B_{ghi}P$	1:2,000	25	320–389	0.27[e]
$B_{ghi}P$	1:1,000	125		
Cor	1:5,000	25	276–311	1.04[f]
Cor	1:4,000	125		

Notes. [a] The wavelength intervals are those used for integrating the strongest neutral PAH absorption band systems. [b] The oscillator strengths are listed for the strongest neutral absorption bands and are taken from the literature: [c] Gudipati (1993), [d] Bito et al. (2000); Wang et al. (2003), [e] Rouillé et al. (2007), [f] Ehrenfreund et al. (1992).

its cationic species is assumed to occur during the first photolysis stage:

$$PAH \xrightarrow{VUV} PAH^+ + e^-. \tag{2}$$

Linear fits are made to the first data points, and the slope directly reflects the oscillator strength of the cation relative to that of the neutral molecule. None of the PAH species in our sample substantially deviates from a one-to-one conversion during the first 100 s of photolysis, making the assumption valid and the resulting relative oscillator strength values reliable starting points for further analysis.

Figure 2 shows typical absorption spectra for the 25 K PAH:H_2O ice mixtures taken at the maximum cation absorption. The position of the band origin, the range used for integration and oscillator strength value relative to the strongest neutral absorption are listed in Table 2. The assignments of the neutral and photoproduct bands are discussed for each individual PAH below.

Table 2. Overview of the studied PAHs, the corresponding state symmetry, position of the band origin, the range over which a band profile is integrated, and relative cation oscillator strength[a].

Species	Symmetry	Origin Pos. (nm)	range (nm)	$f_{rel.}$
Ant	$^1B_{2u}$ [b]	375.4	316–385	1.00
Ant$^+$	^2A_u [c]	719.6	505–753	0.74
Ant$^+$	$^2B_{1u}$ [c]	351.1	349–354	0.15
Ant$^+$	^2A_u [c]	313.7	307–318	0.37
Py	$^1B_{2u}$ [d,e]	334.0	290–345	1.00
Py$^+$	$^2B_{1u}$ [d,e]	363.2	350–370	0.13
Py$^+$	^2A_u [d,e]	445.6	411–470	0.99
Py$^+$	$^2B_{1u}$ [d,e]	490.1	...	...
PyH$^.$	...	399.4	380–410	0.26
$B_{ghi}P$	$^1B_2$ [f]	379.8	320–389	1.00
$B_{ghi}P^+$	$^2B_1$ [g]	762.2	720–788	0.13
$B_{ghi}P^+$	$^2B_1$ [g]	509.7	451–533	1.10
$B_{ghi}P^+$	$^2A_2$ or $^2B_1$	404.3	390–410	0.13
Cor	$^1B_{1u}$	337.6	320–341	0.17
Cor	$^1E_{1u}$	301.4	276–311	1.00
Cor$^+$	$^2B_{1,2g}$ [g]	687.1	630–760	0.20
Cor$^+$	$^2B_{1,2g}$ [g]	463.7	389–473	0.23
Cor$^+$	?	362.5	352–370	0.16

Notes. [a] Cation oscillator strengths are listed relative to the oscillator strength of the strongest neutral absorption band system. [b] Bak et al. (2000), [c] Szczepanski et al. (1993), [d] Halasinski et al. (2005), [e] Vala et al. (1994), [f] Rouillé et al. (2007), [g] indicates a tentative assignment based on theoretical calculations presented here.

3.1. Anthracene ($C_{14}H_{10}$)

The negative signal between ∼310 and 380 nm (Fig. 2a) is assigned to the $^1B_{2u} \leftarrow {}^1A_g$ Ant transition (Bak et al. 2000) and is caused by the photodestruction of neutral Ant molecules. The positive absorption features are caused by species that are produced from the parent PAH. A vibronic progression arises between 500 and 760 nm with its maximum at 719.6 nm. This progression has previously been assigned to the $^2A_u \leftarrow {}^2B_{2g}$ transition of the singly ionized Ant species (Ant$^+$) in an argon matrix (Szczepanski et al. 1993). For this transition we derive an oscillator strength value of 0.59 relative to that of the neutral. A sharp and strong absorption feature previously assigned to the $^2B_{1u} \leftarrow {}^2B_{2g}$ transition of Ant$^+$ appears at 351.1 nm. This absorption has a relative oscillator strength of 0.15. Likewise, an absorption feature which is assigned to the $^2A_u \leftarrow {}^2B_{2g}$ transition of Ant$^+$ is found at 313.7 nm.

Two additional absorptions are apparent in the spectra of our photolyzed sample. One sharp absorption appears around 445.8 nm and is probably due to photolysis of small Py contaminations in our ice sample, resulting in a Py$^+$ absorption. Additionally, a broad feature spanning the range from 380 to 470 nm is found. This band does not correlate with the cation features and is hence thought to be caused by a mixture of Ant+H and/or Ant+OH addition reaction products. These reaction products have previously been identified mass spectrometrically in VUV photolyzed Ant:H_2O (1:≥100) mixtures (Ashbourn et al. 2007). Also, mid-IR absorption bands were reported in Paper I (Bouwman et al. 2011) that point to the existence of such species in photolyzed ices.
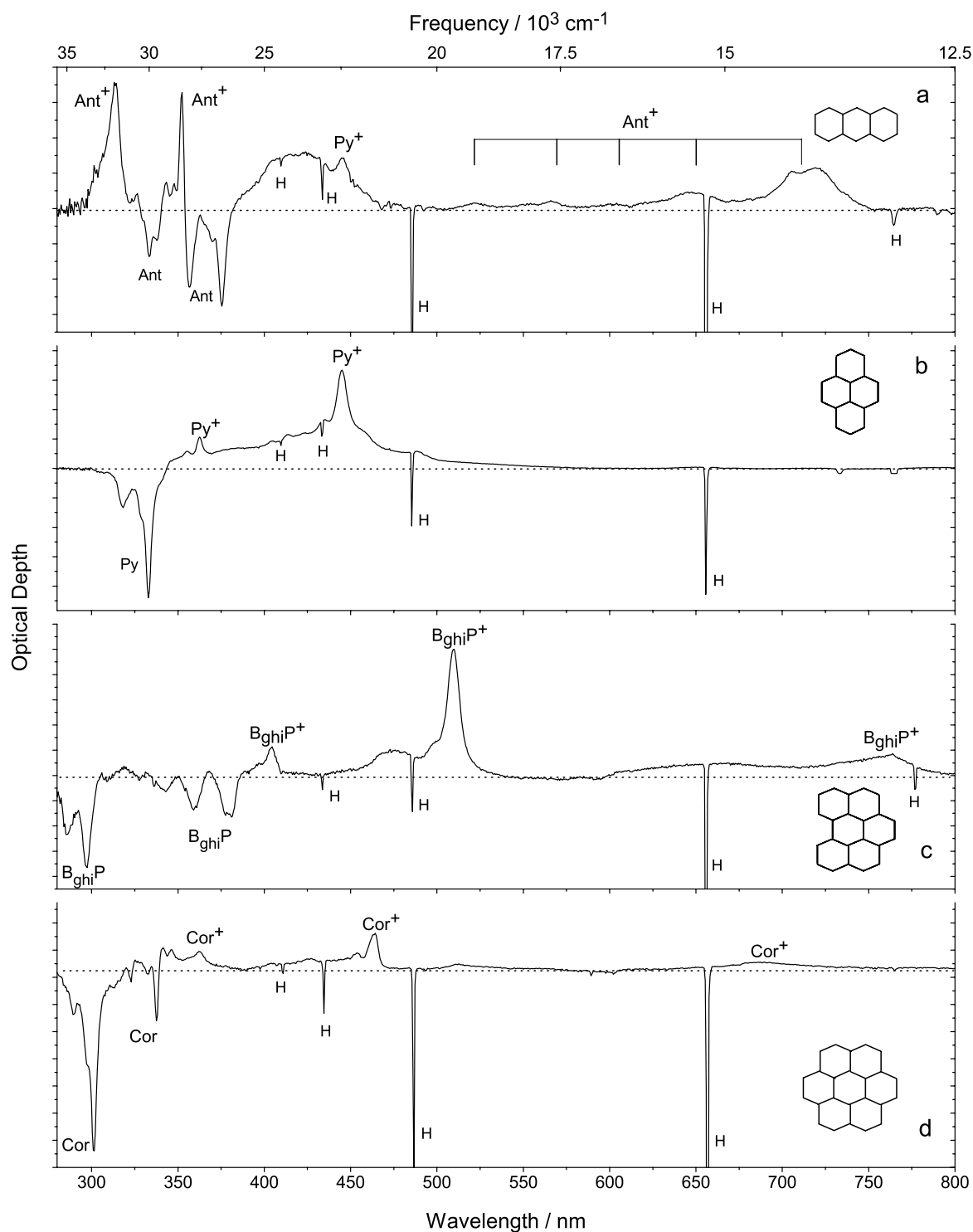
Fig. 2. The 280 to 800 nm spectra of the PAHs anthracene **a)**, pyrene **b)**, benzo[ghi]perylene **c)**, and coronene **d)** in H_2O ice, photolyzed at 25 K. Negative features indicate that the corresponding band carrier is destroyed, positive bands indicate that a species is formed. Hydrogen emission lines (sharp negative signals) originating from the VUV lamp are labeled with an H. The mixing ratios are 1:700, 1:5.000, 1:2.500, and 1:4.000 (PAH:H_2O) for anthracene, pyrene, benzo[ghi]perylene, and coronene, respectively. The molecular structures are indicated in the corresponding spectra. Note that the y-axes for the different spectra are adjusted to facilitate the display and consequently band intensities of different species cannot be directly compared.

3.2. Pyrene ($C_{16}H_{10}$)

The VUV photolysis of Py:H_2O mixtures has been described in detail by Bouwman et al. (2010). Here the band assignments are briefly described for completeness.

The negative bands that appear between 290 and 345 nm are assigned to the $^1B_{2u} \leftarrow {}^1A_g$ electronic transition of neutral pyrene ($S_2 \leftarrow S_0$) (Vala et al. 1994; Halasinski et al. 2005). Most of the positive bands that form upon VUV photolysis of the Py containing H_2O ice are ascribed to the Py$^+$ species. The system ranging

from ~411–470 nm is the strongest Py^+ transition and assigned as $^2A_u \leftarrow ^2B_{3g}$. The weaker absorption bands between 350 and 370 nm are assigned to the $^2B_{1u} \leftarrow ^2B_{3g}$ Py^+ vibronic transition. Finally, the band on the red-wing of the strongest Py^+ transition, situated around 490.1 nm, is due to the $^2B_{1u} \leftarrow ^2B_{3g}$ transition. Besides the rather strong Py cation absorptions, two weak bands which do not correlate with the cation features are detected around 400 and 405 nm. The band at 400 nm has been previously found to originate from an electronic transition in PyH^- and the band at 405 nm has been tentatively assigned to an electronic transition of ^3Py (Bouwman et al. 2010).

3.3. Benzo[ghi]perylene ($C_{22}H_{12}$)

The negative bands between ~280 and 390 nm in the spectrum of the VUV photolyzed $B_{ghi}P:H_2O$ reflect the loss of $B_{ghi}P$. The absorption bands have previously been assigned to the $S_2(^1B_2) \leftarrow S_0(^1A_1)$ transition (Rouillé et al. 2007). In turn, new bands appear upon VUV photolysis of the $B_{ghi}P$ containing H_2O ice. A very strong absorption, which has previously been assigned to a $B_{ghi}P^+$ absorption by Salama et al. (1995) arises at 509.7 nm. Another, much weaker, absorption appears in the mid-IR at 762.2 nm. This band has been assigned in previous argon matrix work to a low energy electronic transition of the $B_{ghi}P^+$ species (Hudgins & Allamandola 1995). Here we report a new absorption band at 404.3 nm, which shows a clear correlation with the other $B_{ghi}P^+$ absorptions. This band is likely due to a higher electronic state of $B_{ghi}P^+$.

An attempt has been made to assign the new observed cation transitions by means of DFT calculations. The optimized geometry of the $B_{ghi}P$ cation has C_{2v} symmetry. The calculations are based on the molecule in the x–z plane with the z-axis coinciding with the C_2 symmetry axis. The electronic ground state is $^2A_2$ making dipole-allowed transitions to A_2, B_2, and B_1 states possible. In the observed wavelength range, several transitions are predicted by TDDFT calculations. A transition to a $^2B_1$ state is calculated to be at 673 nm ($f_{calc.} = 0.048$), which may correspond to the observed band at 762.2 nm. Another transition calculated at 472 nm ($f_{calc.} = 0.21$) is relatively close in energy to the strongest observed band at 509.7 nm and we tentatively attribute this to the corresponding transition also involving a $^2B_1$ state. The absorption at 404.3 nm corresponds with a transition either to the $^2A_2$ or to the $^2B_1$ state. The calculations also predict a transition to the $^2A_2$ state around 300 nm, which overlaps with an absorption from the neutral molecule and consequently cannot be discriminated.

3.4. Coronene ($C_{24}H_{12}$)

The neutral Cor molecule is of D_{6h} symmetry. From the A_{1g} ground state, dipole-allowed transitions are only possible to electronic states of A_{2u} or E_{1u} symmetry. The observed absorption spectrum in cryogenic inert gas matrices strongly resembles the spectrum of hexa-peri-hexabenzocoronene (HBC, Rouillé et al. 2009). The weak $S_1(^1B_{2u}) \leftarrow S_0(^1A_{1g})$ transition expected near 390 nm is not seen in our spectrum, but the $S_2(^1B_{1u}) \leftarrow S_0(^1A_{1g})$ transition appears at 337.6 nm. As with HBC, it gains intensity due to vibronic interaction with the first allowed transition $S_3(^1E_{1u}) \leftarrow S_0(^1A_{1g})$ found at 301.4 nm. The TDDFT calculations predict this transition at 303 nm ($f_{calc.} = 1.3$).

As already noted by Oomens et al. (2001), the degenerate ground state of the coronene cation causes Jahn-Teller interaction and leads to an effective reduction of the point group from

D_{6h}, as found for the neutral species, to D_{2h}. It also complicates the assignment of measured absorption bands on the basis of DFT calculations. However, the DFT geometry optimization predicts a slightly elongated structure for the coronene cation with an elongation of only 0.7% of the total diameter. Therefore, we can only provide tentative band assignments assuming D_{2h} to be the correct point group. In that case, the electronic ground state is $^2B_{3u}$. The feature seen in H_2O ice at 463.7 nm corresponds with a transition to an excited state of $B_{1,2g}$ symmetry. This band was found at 462 nm in an Ar matrix (Szczepanski & Vala 1993) and at 459 nm in a Ne matrix with an oscillator strength of 0.012 (Ehrenfreund et al. 1992). The calculation predicts three states between 390 nm and 460 nm with somewhat higher oscillator strengths between 0.02 and 0.05. Likewise, the broad cation absorption at 687.1 nm could belong to transitions to states of $B_{1,2g}$ symmetry. Further dipole-allowed transitions to $B_{1,2g}$ electronic states are predicted around 310 nm, overlapping with the strongest absorption of neutral Cor. These bands are probably very broad, leading to a rise in the baseline around 310 nm as visible in Fig. 2.

4. PAH ionization rates

The previously derived oscillator strength of the strongest cation band relative to that of the strongest neutral parent PAH transition (Fig. 1) is now used for quantification of the reaction channels that are driven by the VUV photolysis. The evolution of the column density in the ice is tracked as a function of time. As stated earlier, this is far more accessible in the optical work presented here than in the infrared work (Paper I). Cation relative oscillator strengths are used to convert the integrated absorbance into a column density relative to the amount of the neutral species. The analysis is based on the strongest cation bands listed in Table 2. The resulting time evolution of the number densities, relative to the deposited amount of neutral PAH, is shown in Fig. 3 for the four systems studied here.

In the analysis we consider a channel for ionizing the PAH with rate k_{11}, a back-channel for recombination of PAH^+ species with electrons with rate k_{12}, a channel for the formation of products P_1 directly from the parent neutral PAH with rate k_1, and the formation of products P_2 from the PAH^+ species with rate k_2. The reaction scheme is schematically displayed in Fig. 4. This reaction scheme effectively describes the processes observed in the laboratory experiment for a binary $PAH:H_2O$ ice mixture. Caution is needed when using the reaction rate constants derived here in an astrochemical model, since the measurements are performed for specific binary mixtures only. For the $Py:H_2O$ sample, a reaction scheme with one more channel was used in Bouwman et al. (2010) since this molecule clearly follows an additional reaction path involving PyH^-. The contribution of PyH^- to the total amount of reaction products is low and for the sake of consistency all data, including pyrene, are fitted with the same rate equations following from the reaction scheme indicated in Fig. 4.

The time-dependent chemistry of PAHs in H_2O ice is studied for two temperatures, 25 K and 125 K. The fits are co-plotted with the experimental data (left and right column of Fig. 3, respectively). Fits to the time evolution curve of the PAH with the strongest cation absorption, $B_{ghi}P$, are made twofold; keeping the ionization channel, k_{11}, temperature dependent and temperature independent. This yields insight in the effect of the temperature on the process. In our previous publication (Bouwman et al. 2010) we noted a temperature dependence in the Py ionization channel. In the case of Py^+, the signal is very weak and

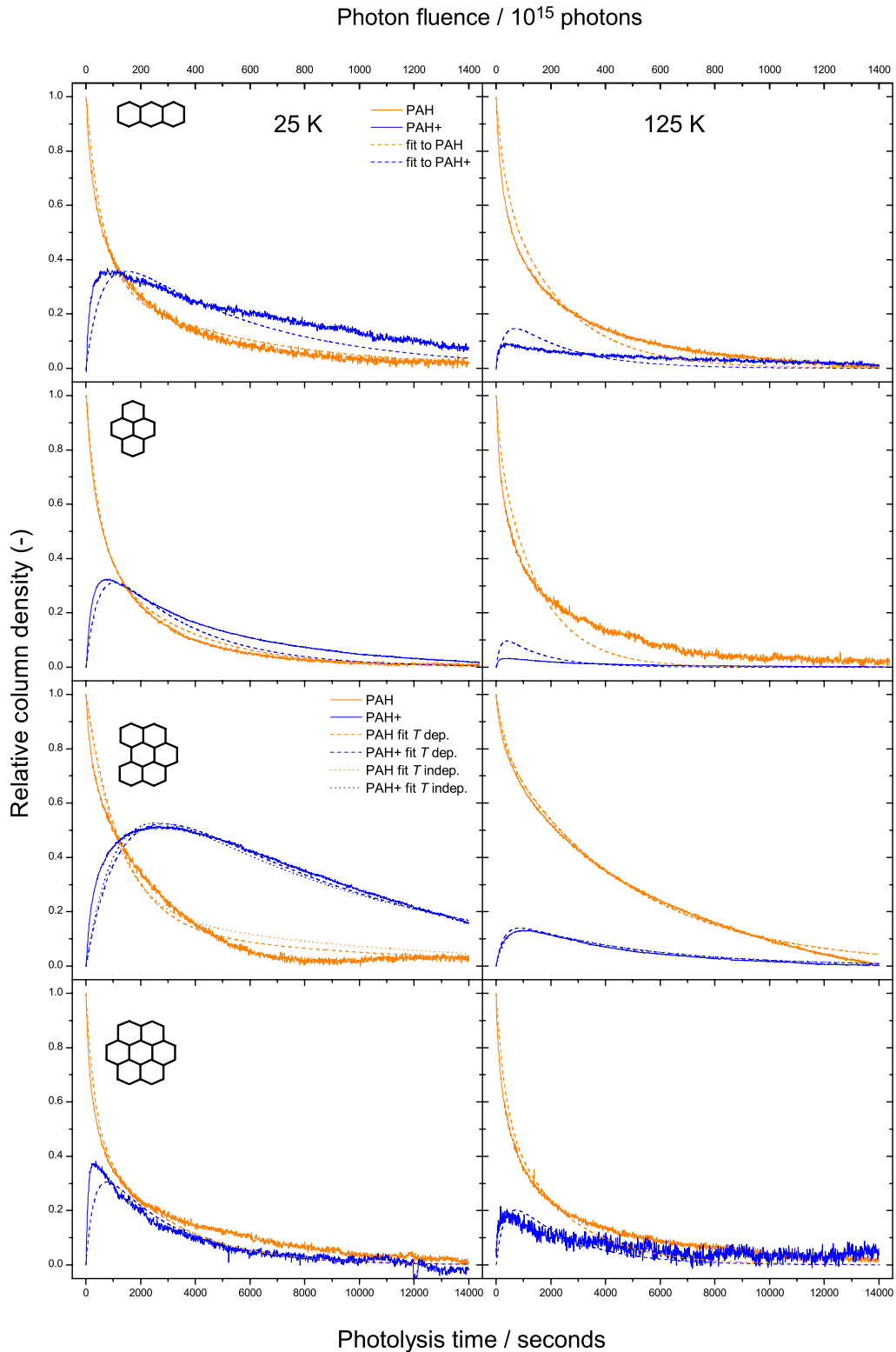Photon fluence / 10^{15} photons

Fig. 3. Neutral PAH decay and the rise and fall of the corresponding cation signals for the four PAHs, anthracene **a)**, pyrene **b)**, benzo[ghi]perylene **c)**, and coronene **d)** trapped in H_2O ice for two different temperatures (*left* – 25 K and *right* – 125 K) as a function of VUV photolysis time. The molecular structure and fitted curves (derived from the model in Fig. 4) are indicated in the plots as well.

thus an accurate fit is hard to obtain. From the two fits to the $B_{ghi}P$ data in Fig. 3 (both T-dependent and T-independent) it is clear that temperature actually does not have a large influence on the quality of the fit, and inherently the ionization rate k_{11} turns out to be independent of temperature. The ionization rate

k_{11} of the other species, Ant and Cor, also does not exhibit a large temperature dependence. Table 3 gives an overview of the fit parameters which are obtained while keeping all parameters free, i.e. dependent of temperature. The photoionization rate (k_{11}) and recombination rate (k_{12}) are in agreement with previously
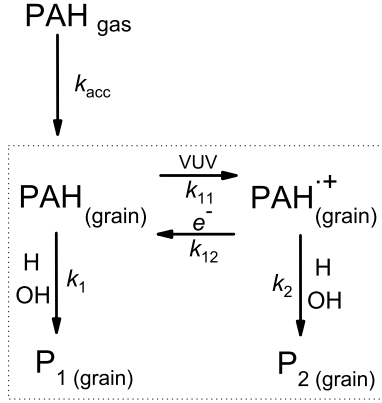
Fig. 4. The reaction scheme used to fit the experimental time evolution of PAHs, their cations and other photoproducts upon VUV irradiation is indicated in the dotted box. The total reaction scheme including the accretion of PAH species from the gas phase into the ice is used for modeling the astrophysical case as described in Sect. 5.

Table 3. Fit parameters obtained by fitting the experimental time evolution of species (Fig. 3) following the reaction scheme indicated in Fig. 4.

Species	Temp (K)	k_{11}	k_{12}	k_1	k_2
Ant	25	8	6	4	0.8
Ant	125	7	20	6	0
Py	25	10	8	4	3
Py	125	8	50	8	0
$B_{ghi}P$	25	7	2	0.8	1
$B_{ghi}P$	125	4	20	2	1
Cor	25	10	20	5	2
Cor	125	9	20	7	0

Notes. All reaction rates are in units of 10^{-4} s^{-1}.

published rates, while product formation rates show significant differences (Bouwman et al. 2010; Gudipati & Allamandola 2003).

From the constants in Table 3 it is found that the recombination channel, k_{12}, increases with temperature, except in the case of Cor. The rate of product formation directly from the parent PAH, k_1, exhibits some temperature dependence. In the case of Ant:H_2O and Cor:H_2O photolysis it increases by a factor of ~1.5 and for Py and $B_{ghi}P$ it increases by a factor of 2. This behavior indicates that reactions of a PAH molecule with H_2O ice photoproducts – H and OH – become more efficient at higher temperatures, presumably because of a larger mobility of these species. The formation rate of products from cation species, k_2, on the other hand, drops to zero at 125 K for all PAHs except for $B_{ghi}P$. What is most striking about the data presented in Table 3, is that the ionization rate (k_{11}) for *all* PAHs is of the same order.

By the end of an experiment, typically after about 14 000 s of VUV photolysis, both the neutral parent PAH and the cation features disappear. They are replaced with other absorptions superposed on the baseline, but there is no clear spectral signature which can be compared to literature data on possible photoproducts. In Paper I more clear signatures of photoproducts were found, which were tentatively assigned to fundamental vibrations of functional groups in the newly formed photoproduct species (PAH–X_n, with X being H, O, or OH). It is likely that similar photoproducts are formed in the experiments described here.

5. Astrophysical implications

As indicated by the rate constants in Table 3, PAH ionization is an efficient process in VUV irradiated PAH containing H_2O ice for the laboratory conditions studied here. This was already known for Py, but is found here to be the case for several other PAHs as well. The largest molecule in our sample, Cor, contains 24 carbon atoms, which is still small from an astrophysical viewpoint. However, the experimental study presented here indicates that the ionization rate is size independent in the range of species investigated. We extend our findings to the astrophysical case, in which larger PAH species ($N_C \geq 50$) are thought to be most relevant. Although additional experiments are needed to verify that these rates are indeed size independent, we assume for the moment that the rates reported here provide a good estimate for the larger species. This is sufficient to derive a first order approximation on the photoprocessing rates of PAHs in an interstellar ice.

Here, we discuss the relevance of PAH:H_2O ice chemistry in clouds where $A_V \geq 3$ mag, the magnitude found for the onset of the 3 μm interstellar H_2O ice absorption band (Whittet et al. 2001). In a previous paper (Bouwman et al. 2010) we have estimated the rate of photoprocessing of PAHs versus photodesorption of the main mantle species using the recent water photodesorption results obtained by Öberg et al. (2009b). We concluded there that for $A_V = 3$ mag the role of photoionization of PAHs in the mantle is of the same order as that of the photodesorption of the mantle species. Since interstellar extinction attenuates the hard UV required for photodesorption ($\lambda \leq 140$ nm) far more than the radiation sufficient to ionize PAHs in H_2O ice ($\lambda \approx 310$ nm (Gudipati 2004; Woon & Park 2004)), even for the typical interstellar radiation field (Habing 1968), PAH:H_2O photochemical processes are expected to take place. This effect increases in importance as the cloud density increases. In the following we put the measured reaction rates described in Sect. 4 into their astrochemical context.

In the diffuse interstellar medium (PDRs), PAHs are initially in the gas phase. The formation of PAH photoproducts on grain mantles therefore requires two steps: the neutral PAHs must first freeze out from the gas phase onto the grains where they can then participate in solid state reaction networks. The rate of accretion of a PAH species onto a grain, R_{acc}^{ISM}, is given by

$$
\begin{aligned}
R_{acc}^{ISM} &= v_{PAH} n_{grain} \left(\pi a^2 \right) n_{PAH} \\
&= \sqrt{\frac{8k}{\pi}} \frac{n_{grain}}{n_H} \left(\pi a^2 \right) \sqrt{\frac{T_{gas}}{M}} n_H n_{PAH} \\
&= 4.57 \times 10^{-8} \sqrt{\frac{T_{gas}}{M}} n_H n_{PAH} \\
&= k_{acc} n_H n_{PAH},
\end{aligned}
$$ (3)

with v_{PAH} the velocity of the PAH molecule in the gas phase, n_{PAH} the gas phase number density of PAHs, n_H the total number density of hydrogen, $\frac{n_{grain}}{n_H}$ the dust to gas number ratio (10^{-12}), a the standard grain radius (0.1 μm), T_{gas} the gas temperature, M the molecular mass of the PAH molecule (in amu), and k_{acc} the accretion rate (in cm^3 s^{-1}). Additionally, all measured PAH reaction coefficients, k^{lab}, are scaled to the interstellar photon flux and the extinction of the cloud by

$$
k^{ISM} = k^{lab} \left(\frac{\Psi_{ISM}}{\Psi_{lab}} \exp\left[-\gamma A_V \right] + \frac{\Psi_{CR}}{\Psi_{lab}} \right),
$$ (4)

with k^{lab} the measured ionization rate constant (s^{-1}), Ψ_{ISM} the interstellar UV flux (10^8 photons cm^{-2} s^{-1} from Shen et al. 2004),
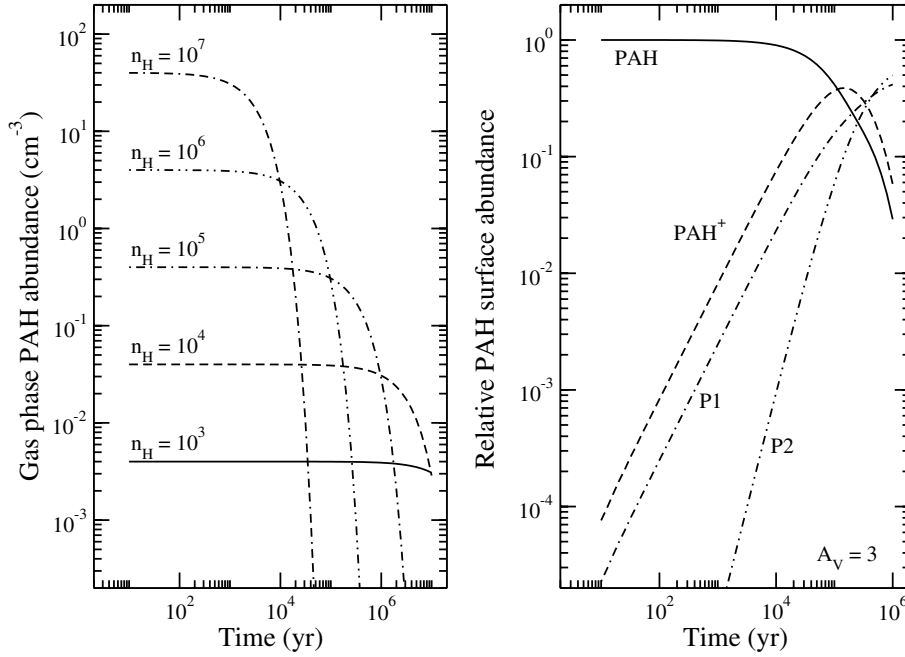
Fig. 5. *Left panel*: modeled depletion of gas phase PAHs on cold interstellar grains as a function of cloud density. *Right panel*: modeled time-dependent PAH loss and PAH photoproduct growth in a PAH:H_2O ice mantle within a cloud experiencing $A_V = 3$ mag of visual extinction. It is explicitly assumed that H_2O ice photodesorption is not efficient enough to act rate limiting.

Ψ_{lab} the laboratory VUV flux, γ a measure of UV extinction relative to visual extinction (≈ 2) (Roberge et al. 1991), A_V the visual magnitude, and Ψ_{CR} the cosmic ray induced photon flux.

An initial total gas phase PAH abundance of 4% with respect to H_2O and an abundance of H_2O of 10^{-4} with respect to n_H is assumed. We further use the largest PAH investigated in this study, Cor, as a prototype system, which results in $M = 300$ amu, leaving T_{gas}, n_H, and A_V as input parameters for the model.

The timescale at which PAHs freeze out onto the grains is investigated first. The left panel of Fig. 5 plots the gas phase PAH abundance for different initial densities n_H. The graph clearly shows that for a dense cloud with $n_H = 10^3$ cm^{-3}, it takes more than 10^7 years for the gas phase to become depleted of PAHs, far longer than the few million year lifetime of a typical molecular cloud. Densities of 10^5 cm^{-3} and higher need to be reached for PAH freeze out to occur on a reasonable timescale. The reason for this is that at low densities the frequency with which PAHs encounter a grain is very low, since the grain abundance directly scales with density. Furthermore, the accretion rate scales with the velocity of the species and inherently with its mass. PAH molecules are heavy molecules and thus move slowly through the cloud, thereby slowing down their depletion process. Once the PAH does encounter a cold grain, the sticking probability is high and, since PAHs are non-volatile molecules, they will remain in the ice as long as the ice matrix remains.

At such high densities, however, the interstellar radiation field is almost fully attenuated and only cosmic ray induced photons play a role. This is not enough to drive significant PAH photoprocessing within a reasonable time. However, in Bouwman et al. (2011) we have shown for the high-mass Young Stellar Object (YSO) W33A and the low-mass YSO RNO 91 that the ice mantle may contain between 2–3% of PAH photoproducts with respect to H_2O. In order for this to have occured, these high PAH photoproduct concentrations must have been formed under the influence of a strong radiation field local to the embedded protostar. The plot in the right panel in Fig. 5 shows the PAH ice

chemistry as a function of time under the standard interstellar radiation field at 3 mag (right panel). The model starts with PAHs frozen out onto the grains. The neutral PAH and the photoproduct abundances are given with respect to the total PAH abundance. For $A_V = 3$ mag the formation of significant amounts of photoproducts is after about 10^5 yrs.

Consequently, to explain the high abundances of frozen PAH photoproducts reported in Bouwman et al. (2011), grains first must be in a high density environment after which they are exposed to a high UV field. These conditions can be met with the following scenario for both the high- and low-mass YSOs W33A and RNO 91: the PAH:H_2O ices form in the pre-collapse, high density phase. Once the newly formed star starts radiating UV photons, ice covered grains in the vicinity of the star will be exposed to the UV field. In protoplanetary disks, a similar situation can occur due to vertical mixing. The ice covered dust grains form in dense regions around the mid-plane. Vertical mixing brings them closer to the warmer top layer of the disk and back down towards the cold mid-plane of the disk.

Due to a lack of laboratory studies on the frequency dependency of PAH ionization and water photodesorption, it is hard to put both processes in direct perspective. Water photodesorption was shown to be effective for Lyman-α radiation (Öberg et al. 2009b) and one may argue that water is photodesorbed before PAH photo-ionization starts to play a role. The number of PAH ionizing photons, however, is expected to be larger (as ionization also takes place for lower energies) and, in addition, PAH ionization energies are lowered in water ice (Gudipati & Allamandola 2004). Therefore, we expect that PAH ionization is a process that should not be neglected a priori. The data presented here, actually, offer a way to search for PAH$^+$ signatures in the solid state, paving the way to answer the question to which extend PAH ionization in the solid state will be relevant. Indeed, optical depths for Py and Py$^+$ in the near UV/VIS have been estimated to amount to $0.01 \leq \tau \leq 0.06$ towards MWC297 (Bouwman et al. 2009) and the information listed in Table 2

provides the means for an optical detection of PAH/PAHs$^+$ in the solid state. The corresponding electronic transitions are more unique than the infrared signatures, and consequently overlapping spectra will not add up; in the end, individual contributions may turn out to be small.

6. Conclusions

The work presented here describes photolysis experiments on interstellar H_2O ice samples containing four different PAHs: Ant, Py, B$_{ghi}$P, and Cor. UV, visible and near-IR band positions for PAH and PAH derivatives have been determined in a H_2O ice matrix. Furthermore, oscillator strengths of the PAH$^+$ species have been derived for all the PAH$^+$ electronic transitions relative to those of the neutral parent PAH molecule. The temporal evolution of cation production is tracked for the four PAHs at the two temperatures, 25 and 125 K. Experimental data are fitted to a reaction network and the resulting rate constants are used in a first-order time-dependent astrochemical model, including PAH freeze-out and photoprocessing in ices. The main conclusions are:

1. All four PAHs behave similarly upon VUV photolysis in a H_2O ice. The cationic species are quickly and efficiently produced in low temperature ices. The cation number density reaches a maximum and then slowly subsides with photolysis time. The PAH photoionization efficiency decreases in high temperature H_2O ice. This behavior can be attributed to PAH-radical or PAH$^+$-radical reactions being more important due to a larger mobility of radical species (H and OH) in the ice at these temperatures.

2. The PAH and PAH$^+$ photochemical time evolution data have been fitted with a model based on a chemical reaction scheme involving PAH ionization and PAH reactions with radical species. All four PAHs exhibit similar reaction rates, allowing for the general conclusion that PAH photoreaction rates in H_2O ice at low temperatures are size-independent over the range of species studied here.

3. An astrochemical model is applied to estimate the time-dependent freeze-out of PAHs on cold interstellar grains in a dense molecular cloud. Because of their large mass and low number density, this model indicates that PAH depletion is not important on time scales less than 10^6–10^7 years for regions of clouds with densities less than 10^5 cm^{-3}. However, at higher densities PAH freeze out becomes important.

4. The photochemistry of PAH:H_2O ices is modeled for translucent conditions. The model results indicate that, under translucent cloud conditions and in denser embedded regions exposed to the local radiation field of young stellar objects, PAH ionization processes may play a role. The PAH$^+$ data presented here offer spectroscopic information needed to carry out astronomical searches to test this suggestion.

References

Ashbourn, S. F. M., Elsila, J. E., Dworkin, J. P., et al. 2007, Meteorit. Planet. Sci., 42, 2035
Bak, K. L., Koch, H., Oddershede, J., Christiansen, O., & Sauer, S. P. A. 2000, J. Chem. Phys., 112, 4173
Bito, Y., Shida, N., & Toru, T. 2000, Chem. Phys. Lett., 328, 310
Boogert, A. C. A., Pontoppidan, K. M., Knez, C., et al. 2008, ApJ, 678, 985
Bottinelli, S., Adwin Boogert, A. C., Bouwman, J., et al. 2010, ApJ, 718, 1100
Bouwman, J., Paardekooper, D. M., Cuppen, H. M., Linnartz, H., & Allamandola, L. J. 2009, ApJ, 700, 56
Bouwman, J., Cuppen, H. M., Bakker, A., Allamandola, L. J., & Linnartz, H. 2010, A&A, 511, A33
Bouwman, J., Mattioda, A. L., Allamandola, L. J., & Linnartz, H. 2011, A&A, 525, A93
Bregman, J. D., Hayward, T. L., & Sloan, G. C. 2000, ApJ, 544, L75
Brooke, T. Y., Sellgren, K., & Geballe, T. R. 1999, ApJ, 517, 883
Chiar, J. E., Tielens, A. G. G. M., Whittet, D. C. B., et al. 2000, ApJ, 537, 749
Draine, B. T., & Li, A. 2007, ApJ, 657, 810
Draine, B. T., Dale, D. A., Bendo, G., et al. 2007, ApJ, 663, 866
Ehrenfreund, P., D'Hendecourt, L., Verstraete, L., et al. 1992, A&A, 259, 257
Frisch, M. J., Trucks, G. W., Schlegel, H. B., et al. 2009, GAUSSIAN 09 Revision A.2, Gaussian Inc., Wallingford CT
Gerakines, P. A., Schutte, W. A., Greenberg, J. M., & van Dishoeck, E. F. 1995, A&A, 296, 810
Gudipati, M. 1993, Chem. Phys., 173, 143
Gudipati, M. 2004, J. Phys. Chem. A., 108, 4412
Gudipati, M. S., & Allamandola, L. J. 2003, ApJ, 596, L195
Gudipati, M. S., & Allamandola, L. J. 2004, ApJ, 615, L177
Habing, H. J. 1968, Bull. Astron. Inst. Netherlands, 19, 421
Halasinski, T. M., Salama, F., & Allamandola, L. J. 2005, ApJ, 628, 555
Hudgins, D. M., & Allamandola, L. J. 1995, J. Phys. Chem., 99, 3033
Kjaergaard, H. G., Robinson, T. W., & Brooking, K. A. 2000, J. Phys. Chem. A, 104, 11297
Muñoz Caro, G. M., & Dartois, E. 2009, A&A, 494, 109
Muñoz Caro, G. M., Meierhenrich, U. J., Schutte, W. A., et al. 2002, Nature, 416, 403
Öberg, K. I., Boogert, A. C. A., Pontoppidan, K. M., et al. 2008, ApJ, 678, 1032
Öberg, K. I., Garrod, R. T., van Dishoeck, E. F., & Linnartz, H. 2009a, A&A, 504, 891
Öberg, K. I., Linnartz, H., Visser, R., & van Dishoeck, E. F. 2009b, ApJ, 693, 1209
Oomens, J., Sartakov, B. G., Tielens, A. G. G. M., Meijer, G., & von Helden, G. 2001, ApJ, 560, L99
Pontoppidan, K. M., van Dishoeck, E. F., & Dartois, E. 2004, A&A, 426, 925
Roberge, W. G., Jones, D., Lepp, S., & Dalgarno, A. 1991, ApJS, 77, 287
Rouillé, G., Arold, M., Staicu, A., et al. 2007, J. Chem. Phys., 126, 174311
Rouillé, G., Steglich, M., Huisken, F., Henning, T., & Müllen, K. 2009, J. Chem. Phys., 131, 204311
Salama, F., Joblin, C., & Allamandola, L. J. 1995, Planet. Space Sci., 43, 1165
Sellgren, K., Brooke, T. Y., Smith, R. G., & Geballe, T. R. 1995, ApJ, 449, L69
Shen, C. J., Greenberg, J. M., Schutte, W. A., & van Dishoeck, E. F. 2004, A&A, 415, 203
Smith, J. D. T., Draine, B. T., Dale, D. A., et al. 2007, ApJ, 656, 770
Smith, R. G., Sellgren, K., & Tokunaga, A. T. 1989, ApJ, 344, 413
Szczepanski, J., & Vala, M. 1993, ApJ, 414, 646
Szczepanski, J., Vala, M., Talbi, D., Parisel, O., & Ellinger, Y. 1993, J. Chem. Phys., 98, 4494
Tielens, A. G. G. M. 2008, ARA&A, 46, 289
Vala, M., Szczepanski, J., Pauzat, F., et al. 1994, J. Phys. Chem., 98, 9187
Wang, B. C., Chang, J. C., Tso, H. C., Hsu, H. F., & Cheng, C. Y. 2003, J. Mol. Struct. (Theochem), 629, 11
Whittet, D. C. B., Gerakines, P. A., Hough, J. H., & Shenoy, S. S. 2001, ApJ, 547, 872
Woon, D. E., & Park, J.-Y. 2004, ApJ, 607, 342